Peng Wang

Wei Gao

Zhiyi Cao

Kenneth M. Liechti

Rui Huang[1]

e-mail: ruihuang@mail.utexas.edu

Department of Aerospace Engineering
and Engineering Mechanics,
University of Texas,
Austin, TX 78712

Numerical Analysis of Circular Graphene Bubbles

Pressurized graphene bubbles have been observed in experiments, which can be used to determine the mechanical and adhesive properties of graphene. A nonlinear plate theory is adapted to describe the deformation of a graphene monolayer subject to lateral loads, where the bending moduli of monolayer graphene are independent of the in-plane Young's modulus and Poisson's ratio. A numerical method is developed to solve the nonlinear equations for circular graphene bubbles, and the results are compared to approximate solutions by analytical methods. Molecular dynamics simulations of nanoscale graphene bubbles are performed, and it is found that the continuum plate theory is suitable only within the limit of linear elasticity. Moreover, the effect of van der Waals interactions between graphene and its underlying substrate is analyzed, including large-scale interaction for nanoscale graphene bubbles subject to relatively low pressures. [DOI: 10.1115/1.4024169]

1 Introduction

Nanoscale graphene bubbles were observed when mechanically exfoliated graphene flakes were deposited on a SiO_2/Si substrate and subjected to irradiation of energetic protons [1]. Much larger graphene bubbles were observed when the graphene flakes were exposed to vapors of hydrofluoric acid (HF) and water (H_2O). In both cases, gas molecules were released from the substrate and trapped underneath the impermeable graphene membranes, resulting in the formation of the nano-to-microscale bubbles. A recent study reported that graphene bubbles are regularly found in large graphene flakes obtained by mechanical cleavage and placed on SiO_2/Si substrates [2]. The observed graphene bubbles have diameters ranging from tens of nanometers to tens of microns, with a variety of shapes (circular, triangular, and diamond). Bubbles have also been observed for graphene grown on metals, such as Pt (111) [3] and Ru (0001) [4]. While the formation of graphene bubbles may depend on the material systems and experimental conditions, several potential applications of the graphene bubbles have been proposed. For example, the use of graphene nanobubbles has been suggested as a viable method for strain engineering to manipulate the electronic properties of graphene [3,4]. Controllable curvature of graphene bubbles has been demonstrated by applying an external electric field [2], potentially allowing their use as optical lenses with variable focal length. Microscale graphene bubbles have been used to study the Raman spectrum of graphene under biaxial strain [5]. Pressurized graphene bubbles on patterned substrates were used to demonstrate the impermeability of graphene to gas molecules [6], to measure elastic properties of graphene and the adhesion energy between graphene and silicon oxide [7].

In a previous study [8], analytical methods were employed to deduce the interfacial adhesion energy from measurements of the bubble size (diameter and height). It was found that membrane theory is sufficient for relatively large bubbles of monolayer graphene, where the bending stiffness can be neglected. However, an accurate solution to the nonlinear membrane equations can only be obtained numerically [9]. Moreover, for nanoscale graphene bubbles, the effect of bending stiffness may not be negligible, and the van der Waals interactions between graphene and the substrate

have to be accounted for explicitly. In the present study, we present a nonlinear plate theory, adapted for the in-plane and bending properties of monolayer graphene. A numerical method is then developed to solve the nonlinear equations for circular graphene bubbles, subjected to gas pressure and van der Waals interactions. The numerical results are compared to the approximate solutions obtained by analytical methods and to molecular dynamics simulations.

The remainder of this paper is organized as follows: Sec. 2 presents the nonlinear plate theory and the axisymmetric formulation for circular graphene bubbles. Section 3 briefly reviews the approximate solutions from analytical methods. The numerical method based on a finite difference scheme is presented in Sec. 4, followed by a description of the molecular dynamics simulation methodology in Sec. 5. The results are discussed in Sec. 6 and summarized in Sec. 7.

2 A Nonlinear Plate Theory for Monolayer Graphene

2.1 General Formulation. The mechanical behavior of a graphene monolayer can be described by a mixed continuum mechanics formulation mapping a two-dimensional (2D) plane to a three-dimensional (3D) space [10]. The kinematics of deformation is described by an in-plane Green–Lagrange strain tensor and a curvature tensor, both defined with respect to a reference state in 2D (i.e., the ground state of graphene). Under the assumption of relatively small deformation but with moderately large deflection, the in-plane strain and curvature are approximately

$$\varepsilon_{ij} = \frac{1}{2}\left(\frac{\partial u_i}{\partial x_j} + \frac{\partial u_j}{\partial x_i} + \frac{\partial w}{\partial x_i}\frac{\partial w}{\partial x_j}\right) \qquad (2.1)$$

$$\kappa_{ij} = \frac{\partial^2 w}{\partial x_i \partial x_j} \qquad (2.2)$$

where the Latin subscripts (i or j) take values 1 or 2 for the in-plane coordinates, u_1 and u_2 are the in-plane displacements, and w is the lateral deflection.

The elastic property of graphene is nonlinear and anisotropic in general [11,12]. Under the condition of small deformation, it is taken approximately as linear and transversely isotropic. In this case, a strain energy density function can be written as

$$\Phi = \Phi_\varepsilon(\boldsymbol{\varepsilon}) + \Phi_\kappa(\boldsymbol{\kappa}) \qquad (2.3)$$

where $\Phi_\varepsilon(\boldsymbol{\varepsilon})$ is the strain energy due to in-plane strain and $\Phi_\kappa(\boldsymbol{\kappa})$ is due to curvature; both are measured per unit area of the graphene monolayer at the ground state (unit: J/m^2) as opposed to energy per unit volume (unit: J/m^3) for a 3D solid.

The linear elastic strain energy density function due to the in-plane strain is

$$\Phi_\varepsilon = \frac{E_{2D}}{2(1+\nu)}\left(\varepsilon_{ij}\varepsilon_{ij} + \frac{\nu}{1-\nu}\varepsilon_{ii}\varepsilon_{jj}\right) = \frac{1}{2}N_{ij}\varepsilon_{ij} \qquad (2.4)$$

where N_{ij} is the in-plane membrane force (or 2D stress)

$$N_{ij} = \frac{\partial \Phi_\varepsilon}{\partial \varepsilon_{ij}} = \frac{E_{2D}}{1+\nu}\left(\varepsilon_{ij} + \frac{\nu}{1-\nu}\varepsilon_{kk}\delta_{ij}\right) \qquad (2.5)$$

Here we have used the 2D Young's modulus E_{2D} and Poisson's ratio ν defined under the condition of uniaxial stress [12,13]. The summation convention is implied for the repeated subscripts, and δ_{ij} is the Kronecker δ.

The strain energy density due to curvature can be written as a function of the two invariants of the curvature tensor [14],

$$\Phi_\kappa = \frac{1}{2}DI_\kappa^2 - D_G II_\kappa = \frac{D-D_G}{2}\kappa_{ii}\kappa_{jj} + \frac{D_G}{2}\kappa_{ij}\kappa_{ij} \qquad (2.6)$$

where the invariants $I_\kappa = \kappa_{ii}$ and $II_\kappa = (\kappa_{ii}\kappa_{jj} - \kappa_{ij}\kappa_{ij})/2$, D and D_G are the two bending moduli corresponding to the mean curvature ($\kappa_m = \kappa_{ii}/2$) and the Gaussian curvature ($\kappa_G = II_\kappa$), respectively. The bending and twisting moments are then obtained as the work conjugates with respect to the curvature components,

$$M_{ij} = \frac{\partial \Phi_\kappa}{\partial \kappa_{ij}} = (D-D_G)\kappa_{kk}\delta_{ij} + D_G\kappa_{ij} \qquad (2.7)$$

Unlike classical plate theory [15], the bending moduli of monolayer graphene are not directly related to the in-plane Young's modulus and Poisson's ratio. Instead, they are determined from atomistic modeling as independent properties [16–20]. As discussed in a previous study [19], the physical origin of the bending moduli of the monolayer graphene is fundamentally different from that in classical plate theory.

With the strain energy density functions, the equilibrium equations and boundary conditions can be developed by the principle of virtual displacements, similar to classical plate theory [15]. The in-plane force equilibrium requires that (assuming no body force)

$$\frac{\partial N_{ij}}{\partial x_j} = 0 \qquad (2.8)$$

and moment equilibrium requires that

$$\frac{\partial^2 M_{ij}}{\partial x_i \partial x_j} - N_{ij}\frac{\partial^2 w}{\partial x_i \partial x_j} = q \qquad (2.9)$$

where q is the lateral loading intensity (e.g., pressure). Substitution of Eq. (2.7) into Eq. (2.9) leads to

$$D\nabla^4 w - N_{ij}\frac{\partial^2 w}{\partial x_i \partial x_j} = q \qquad (2.10)$$

Therefore, under the condition of small in-plane strain and moderately large deflection, a set of nonlinear equations can be used to describe the mechanical behavior of monolayer graphene, which closely resemble the von Karman equations for an isotropic elastic thin plate [15]. The only notable difference lies in the bending moduli of graphene. In particular, we note that it is unnecessary to define a thickness for the graphene monolayer in the 2D continuum formulation. The four basic elastic properties of monolayer graphene have been determined by first-principle calculations and atomistic modeling, as listed in Table 1.

Table 1 Elastic properties of monolayer graphene (DFT, density functional theory; DF-TB, density functional tight-binding; MM, molecular mechanics; REBO, reactive empirical bond-order potential [21]; REBO-2, second-generation REBO potential [22]; AIREBO, adaptive intermolecular REBO potential [23])

Method and reference	E_{2D} (N/m)	ν	D (eV)	D_G (eV)
DFT [16]	345	0.149	1.5	$\cdots$
DFT [12]	348	0.169	$\cdots$	$\cdots$
DF-TB [20]	$\cdots$	$\cdots$	1.61	0.70
MM (REBO) [17,18]	236	0.412	0.83	$\cdots$
MM (REBO-2) [10,19]	243	0.397	1.4	$\cdots$
MM (AIREBO)[a]	277	0.366	1.0	$\cdots$
Experiments [11,25]	342	0.165	$\cdots$	$\cdots$

[a]Based on calculations using LAMMPS [24].

Note that the ratio between the two bending moduli of graphene is $D_G/D = 0.435$ [20], not $(1-\nu)$ as in classical plate theory.

2.2 Axisymmetric Formulation. Consider a circular graphene membrane subjected to axisymmetric loading. The displacements expressed in the polar coordinates are $u_r = u(r)$, $u_\theta = 0$, and $w = w(r)$, where $r = \sqrt{x_1^2 + x_2^2}$. The corresponding in-plane strain components are

$$\varepsilon_r = \frac{du}{dr} + \frac{1}{2}\left(\frac{dw}{dr}\right)^2 \qquad (2.11)$$

$$\varepsilon_\theta = \frac{u}{r} \qquad (2.12)$$

and $\varepsilon_{r\theta} = 0$. The curvature components are

$$\kappa_r = \frac{d^2 w}{dr^2} \qquad (2.13)$$

$$\kappa_\theta = \frac{1}{r}\frac{dw}{dr} \qquad (2.14)$$

and $\kappa_{r\theta} = 0$.

From Eq. (2.5), the radial and circumferential membrane forces are

$$N_r = \frac{E_{2D}}{1-\nu^2}\left(\frac{du}{dr} + \nu\frac{u}{r} + \frac{1}{2}\left(\frac{dw}{dr}\right)^2\right) \qquad (2.15)$$

$$N_\theta = \frac{E_{2D}}{1-\nu^2}\left(\nu\frac{du}{dr} + \frac{u}{r} + \frac{\nu}{2}\left(\frac{dw}{dr}\right)^2\right) \qquad (2.16)$$

The in-plane force equilibrium equation in (2.8) reduces to

$$\frac{dN_r}{dr} + \frac{N_r - N_\theta}{r} = 0 \qquad (2.17)$$

Substitution of Eqs. (2.15) and (2.16) into Eq. (2.17) leads to a nonlinear displacement equation

$$\frac{d^2 u}{dr^2} + \frac{1}{r}\frac{du}{dr} - \frac{u}{r^2} = -\frac{1-\nu}{2r}\left(\frac{dw}{dr}\right)^2 - \frac{dw}{dr}\frac{d^2 w}{dr^2} \qquad (2.18)$$

From Eq. (2.7), the bending moments are

$$M_r = D\frac{d^2 w}{dr^2} + (D-D_G)\frac{1}{r}\frac{dw}{dr} \qquad (2.19)$$

$$M_\theta = (D-D_G)\frac{d^2 w}{dr^2} + \frac{D}{r}\frac{dw}{dr} \qquad (2.20)$$

The moment equilibrium equation in (2.10) is integrated once with respect to r, yielding another nonlinear displacement equation

$$D\left(\frac{d^3w}{dr^3}+\frac{1}{r}\frac{d^2w}{dr^2}-\frac{1}{r^2}\frac{dw}{dr}\right)-\frac{E_{2D}}{1-\nu^2}\frac{dw}{dr}\left(\frac{du}{dr}+\nu\frac{u}{r}+\frac{1}{2}\left(\frac{dw}{dr}\right)^2\right)$$
$$=\frac{1}{r}\int_0^r qrdr \qquad (2.21)$$

Therefore, the axisymmetric problem is to solve the two nonlinear equations in Eqs. (2.18) and (2.21) with prescribed boundary conditions at the edge ($r=a$). In the present study, the lateral load intensity q consists of a constant pressure (p) and the van der Waals (vdW) force between graphene and the substrate, i.e., $q=p-\sigma_{vdW}$, where $\sigma_{vdW}>0$ for attractive force. By a simple model of vdW interactions [26], the vdW force is written as a function of deflection,

$$\sigma_{vdW}(w)=\frac{9\Gamma}{2\delta_0}\left[\left(\frac{\delta_0}{w+\delta_0}\right)^4-\left(\frac{\delta_0}{w+\delta_0}\right)^{10}\right] \qquad (2.22)$$

where δ_0 is the equilibrium separation and Γ is the interfacial adhesion energy. For monolayer graphene on SiO$_2$, experimental measurements have reported values from 0.4 to 0.9 nm for δ_0 [27–29] and from 0.09 to 0.45 J/m^2 for the adhesion energy Γ [7,8,30]. In the present study, we take $\delta_0=0.6$ nm and $\Gamma=0.1$ J/m^2 as typical values and treat the substrate as a rigid surface.

3 Analytical Methods

Several approximate solutions for graphene bubbles were presented in a previous study [8]. They are briefly reviewed here for comparison with the numerical results.

3.1 Linear Plate Solution. For the linear plate analysis, the in-plane strain is assumed to be negligible, and Eq. (2.21) reduces to

$$D\left(\frac{d^3w}{dr^3}+\frac{1}{r}\frac{d^2w}{dr^2}-\frac{1}{r^2}\frac{dw}{dr}\right)=\frac{1}{r}\int_0^r qrdr \qquad (3.1)$$

Subjected to a uniform lateral load ($q=p$) and clamped boundary condition at the edge (i.e., $w=dw/dr=0$ at $r=a$), Eq. (3.1) can be solved analytically by

$$w=h\left(1-\frac{r^2}{a^2}\right)^2 \qquad (3.2)$$

where a is the bubble radius and $h=pa^4/64D$ is the center deflection (bubble height).

3.2 An Approximate Membrane Solution. For a membrane analysis, it is assumed that the bending stiffness is negligible. Thus, the equilibrium equation in (2.21) becomes

$$\frac{E_{2D}}{1-\nu^2}\frac{dw}{dr}\left(\frac{du}{dr}+\nu\frac{u}{r}+\frac{1}{2}\left(\frac{dw}{dr}\right)^2\right)=-\frac{1}{2}pr \qquad (3.3)$$

The two nonlinear membrane equations, (3.3) and (2.18), are coupled and cannot be solved analytically. An approximate solution was developed by the energy method assuming the displacements [8],

$$w=h\left(1-\frac{r^2}{a^2}\right) \qquad (3.4)$$

$$u=u_0\frac{r}{a}\left(1-\frac{r}{a}\right) \qquad (3.5)$$

where $h=\left[\phi(\nu)pa^4/E_{2D}\right]^{1/3}$ and $u_0=\left[\psi(\nu)p^2a^5/E_{2D}^2\right]^{1/3}$, with

$$\phi(\nu)=\frac{75(1-\nu^2)}{8(23+18\nu-3\nu^2)}$$

and

$$\psi(\nu)=\frac{45(3-\nu)^3(1-\nu^2)^2}{8(23+18\nu-3\nu^2)^2}$$

A more accurate membrane analysis was developed by Hencky [9], which included seven terms in the polynomial expansion of the deflection profile (as opposed to the two terms in Eq. (3.4)) with the coefficients determined numerically for specific Poisson's ratios. In particular, for $\nu=0.16$, the center deflection by Hencky's solution is $h=0.687(pa^4/E_{2D})^{1/3}$.

3.3 An Approximate Nonlinear Plate Solution. An energy method was used to develop an approximate solution to the nonlinear plate equations by assuming a deflection profile in form of Eq. (3.2) along with the radial displacement [8]

$$u=r(a-r)(c_1+c_2r) \qquad (3.6)$$

Minimization of the potential energy leads to

$$c_1=\frac{179-89\nu}{126}\frac{h^2}{a^3} \qquad (3.7)$$

$$c_2=\frac{13\nu-79}{42}\frac{h^2}{a^4} \qquad (3.8)$$

$$p=64\eta(\nu)\frac{E_{2D}h^3}{a^4}+64\frac{Dh}{a^4} \qquad (3.9)$$

where

$$\eta(\nu)=\frac{7505+4250\nu-2791\nu^2}{211680(1-\nu^2)}$$

It was shown that the approximate solution converges to the linear plate solution when the bubble height is small ($h<0.1$ nm) but considerably underestimates the pressure when $h>1$ nm [8].

4 A Numerical Method

In this section we present a numerical method to solve the coupled nonlinear equations, (2.18) and (2.21). For convenience we define an effective thickness, $h_e=\sqrt{12(1-\nu^2)D/E_{2D}}$, and normalize the equations using the dimensionless quantities, $\bar{r}=r/h_e$, $\bar{a}=a/h_e$, $\bar{u}=u/h_e$, $\bar{w}=w/h_e$, and $\bar{q}=qh_e^3/D$. In addition, we replace the deflection w with the angle of rotation, $\theta=dw/dr$, and rewrite the equations as

$$g=\frac{d^2\bar{u}}{d\bar{r}^2}+\frac{1}{\bar{r}}\frac{d\bar{u}}{d\bar{r}}-\frac{\bar{u}}{\bar{r}^2}+\frac{1-\nu}{2\bar{r}}\theta^2+\theta\frac{d\theta}{d\bar{r}}=0 \qquad (4.1)$$

$$f=\frac{d^2\theta}{d\bar{r}^2}+\frac{1}{\bar{r}}\frac{d\theta}{d\bar{r}}-\frac{\theta}{\bar{r}^2}-12\theta\left(\frac{d\bar{u}}{d\bar{r}}+\nu\frac{\bar{u}}{\bar{r}}+\frac{\theta^2}{2}\right)-\frac{1}{\bar{r}}\int_0^{\bar{r}}\bar{q}\bar{r}d\bar{r}=0 \qquad (4.2)$$

Next we discretize the equations by the finite difference method with $\Delta\bar{r}=\bar{a}/n$ and $\bar{r}_k=k\Delta\bar{r}$ for $k=0$ to n. At each internal node ($k=1$ to $n-1$), we have

$$g_k = \frac{n^2}{\bar{a}^2}\left(1 + \frac{1}{2k}\right)\bar{u}_{k+1} - \frac{n^2}{\bar{a}^2}\left(2 + \frac{1}{k^2}\right)\bar{u}_k + \frac{n^2}{\bar{a}^2}\left(1 - \frac{1}{2k}\right)\bar{u}_{k-1}$$
$$+ \frac{(1-\nu)n}{2k\bar{a}}\theta_k^2 + \frac{n}{2\bar{a}}\theta_k(\theta_{k+1} - \theta_{k-1}) \tag{4.3}$$

$$f_k = \frac{n^2}{\bar{a}^2}\left(1 + \frac{1}{2k}\right)\theta_{k+1} - \frac{n^2}{\bar{a}^2}\left(2 + \frac{1}{k^2}\right)\theta_k + \frac{n^2}{\bar{a}^2}\left(1 - \frac{1}{2k}\right)\theta_{k-1}$$
$$- \frac{6n}{\bar{a}}\theta_k(\bar{u}_{k+1} - \bar{u}_{k-1}) - \frac{12\nu n}{k\bar{a}}\theta_k\bar{u}_k - 6\theta_k^3 - \xi_k \tag{4.4}$$

where $\xi_k = (\bar{a}/2nk)(\sum_{m=1}^{k-1} 2m\bar{q}_m + k\bar{q}_k)$. When q is a constant, $\xi_k = (k\bar{a}/2n)\bar{q}$. In addition, we have the boundary conditions, $\theta_0 = \theta_n = 0$ and $\bar{u}_0 = \bar{u}_n = 0$.

The Newton–Raphson method is employed to solve the nonlinear equations. We start with the linear plate solution,

$$\theta_k^{(0)} = \frac{\bar{q}k}{16n}\left(\frac{k^2}{n^2} - 1\right)$$

and $\bar{u}_k^{(0)} = 0$, and iterate until a convergence condition is satisfied. At each iteration, the residuals are calculated by Eqs. (4.3) and (4.4) at each node ($k = 1$ to $n-1$), and a correction vector is calculated as

$$\begin{pmatrix} \Delta\boldsymbol{\theta} \\ \Delta\bar{\mathbf{u}} \end{pmatrix} = -\begin{bmatrix} \frac{\partial\mathbf{f}}{\partial\boldsymbol{\theta}} & \frac{\partial\mathbf{f}}{\partial\bar{\mathbf{u}}} \\ \frac{\partial\mathbf{g}}{\partial\boldsymbol{\theta}} & \frac{\partial\mathbf{g}}{\partial\bar{\mathbf{u}}} \end{bmatrix}^{-1} \begin{pmatrix} \mathbf{f} \\ \mathbf{g} \end{pmatrix} \tag{4.5}$$

where $\Delta\boldsymbol{\theta}$ is a vector of $n-1$ components ($\Delta\theta_k$, $k = 1$ to $n-1$) and the same for $\Delta\mathbf{u}$, $\mathbf{f}$, and $\mathbf{g}$. The Jacobian matrix on the right-hand side of Eq. (4.5) consists of four square blocks, each with a rank of $n-1$. This matrix can be readily constructed from Eqs. (4.3) and (4.4). For the convergence criterion, we require that the L2-norm of the relative correction vector is smaller than a specified tolerance, namely

$$|\mathbf{R}| = \left[\sum_{k=1}^{n-1}\left(\Delta\theta_k^2/\theta_k^2 + \Delta u_k^2/u_k^2\right)\right]^{1/2} < \tau \sim 10^{-4} \tag{4.6}$$

If not satisfied, the iteration procedure then repeats with a new approximation, $\theta_k^{(i+1)} = \theta_k^{(i)} + \Delta\theta_k$ and $\bar{u}_k^{(i+1)} = \bar{u}_k^{(i)} + \Delta u_k$.

Subsequently, noting that $\bar{w}_n = 0$ by the boundary condition, we calculate the deflection at each node by numerical integration,

$$\bar{w}_k = -\frac{\bar{a}}{2n}\sum_{m=k}^{n-1}(\theta_m + \theta_{m+1}) \tag{4.7}$$

for $k = 0$ to $n-1$, and the center deflection is then obtained as $h = w_0$. Moreover, we calculate the strain components at each node according to Eqs. (2.11) and (2.12),

$$(\varepsilon_r)_k = \frac{n}{2\bar{a}}(\bar{u}_{k+1} - \bar{u}_{k-1}) + \frac{1}{2}\theta_k^2 \quad \text{and} \quad (\varepsilon_\theta)_k = \frac{n\bar{u}_k}{k\bar{a}} \tag{4.8}$$

for $k = 1$ to $n-1$. At the center ($r = 0$), we have $(\varepsilon_r)_0 = (\varepsilon_\theta)_0 = n\bar{u}_1/\bar{a}$. At the edge ($r = a$), we have $(\varepsilon_r)_n = -n\bar{u}_{n-1}/(2\bar{a})$ and $(\varepsilon_\theta)_n = 0$.

To study the effect of the van der Waals force, we normalize Eq. (2.22) as

$$\bar{\sigma}_{\text{vdW}}(\bar{w}) = \bar{\Gamma}\left[\left(\frac{\bar{\delta}_0}{\bar{w} + \bar{\delta}_0}\right)^4 - \left(\frac{\bar{\delta}_0}{\bar{w} + \bar{\delta}_0}\right)^{10}\right] \tag{4.9}$$

where $\bar{\sigma}_{\text{vdW}} = \sigma_{\text{vdW}}h_e^3/D$, $\bar{\delta}_0 = \delta_0/h_e$, and $\bar{\Gamma} = 9\Gamma h_e^3/(2\delta_0 D)$. After discretization, we have

$$\bar{q}_k = \bar{p} - \bar{\sigma}_{\text{vdW}}(\bar{w}_k) \tag{4.10}$$

where $\bar{p} = ph_e^3/D$ and the deflection $\bar{w}_k$ is given by Eq. (4.7) in terms of the angles θ_m ($m = k$ to $n-1$). Thus, the last term on the right-hand side of Eq. (4.4) becomes a nonlinear function of the angles, which leads to a dense matrix $\partial\mathbf{f}/\partial\boldsymbol{\theta}$. Despite the increased nonlinearity and computational cost, the problem can be solved by the same iterative procedures described above.

In the present study, we focus on monolayer graphene bubbles. Using $E_{2D} = 345$ N/m, $\nu = 0.16$, and $D = 1.5$ eV (or equivalently, 0.238 nN nm), we obtain $h_e = 0.09$ nm. The radii of the graphene bubbles ranges from 10 to 1000 nm, and $n = 1000$ is used for the finite difference discretization. For each bubble radius, the displacements u and w are calculated as the pressure increases.

5 Molecular Dynamics Simulations

A molecular dynamics (MD) method is developed to simulate graphene bubbles using a pressure-transmitting gas. The method is similar to that proposed by Martoňák et al. [31] for pressure-induced structural transformation. Here, gas molecules are inserted between two graphene sheets, as shown in Fig. 1. The carbon atoms of the graphene sheets are fixed except for those inside a circle of a specific radius (e.g., $a = 10$ nm) at the center of the upper graphene sheet, whereas the lower graphene sheet is used to simulate a rigid surface as the substrate. The molecular interactions between the gas and carbon atoms transmit a pressure that pushes up the carbon atoms to form a circular bubble. The separation between the two graphene sheets is sufficiently large (5 nm) so that the interaction between them is negligible. Periodic boundary conditions are applied in the in-plane directions. In the lateral direction, sufficient empty spaces are included in the simulation box, both below the lower graphene sheet and above the upper sheet. The typical size of the simulation box is $24.5 \times 24.5 \times 15$ nm^3. MD simulations are performed in canonical ensemble (NVT) using LAMMPS [24]. We use the Nose–Hoover thermostat to control the temperature and the time step is 0.1 fs.

The carbon-carbon interatomic interaction is described by the second-generation reactive empirical bond-order (REBO-2) potential [22]. The interaction between two gas molecules is described by a repulsive soft-sphere potential energy function [32],
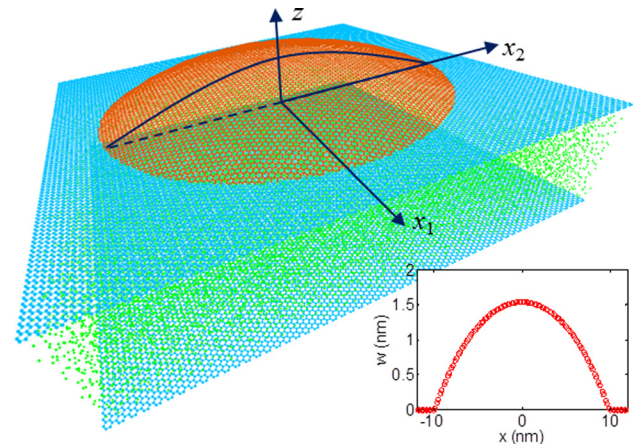

Fig. 1 Molecular dynamics simulation of a graphene bubble (gas molecules are green, fixed carbon atoms are cyan, and mobile carbon atoms are orange). The bubble radius is 10 nm, $N_g = 225,000$, and $T = 300$ K; the pressure is calculated to be 307.4 MPa. The inset shows the deflection profile of graphene along one diameter.

$$U_{g-g}(r) = \xi \left(\frac{\sigma_{g-g}}{r} \right)^{12} \qquad (5.1)$$

where r is the separation between two gas molecules and the two parameters are set as $\xi = 1$ eV and $\sigma_{g-g} = 0.35$ Å. According to the virial theorem [33], the pressure inside a gas can be calculated as

$$p = \frac{N_g k_B T}{V_g} + \frac{\sum_{i=1}^{N_g} \langle \mathbf{r}_i \cdot \mathbf{f}_i^{g-g} \rangle}{3 V_g} \qquad (5.2)$$

where N_g is the total number of the gas molecules, V_g is the volume, k_B is the Boltzmann's constant, T is the temperature, $\mathbf{r}_i$ is the position vector of gas molecule i, $\mathbf{f}_i^{g-g}$ is the molecular force vector acting on the molecule i by the other gas molecules, and $\langle \cdot \rangle$ represents the time average of the enclosed quantity. The molecular force $\mathbf{f}_i^{g-g}$ is calculated from the potential function $U_{g-g}(r)$. The first term on the right-hand side of Eq. (5.2) is the ideal gas law, while the second term takes into account the intermolecular potential energy. We used argon (Ar) as the gas molecules in the MD simulations.

The interaction between a gas molecule and a carbon atom in graphene is also described by a repulsive potential energy function, $U_{g-c}(r) = \xi \left(\sigma_{g-c}/r \right)^{12}$, where we set $\xi = 1$ eV and $\sigma_{g-c} = 1.39$ Å. These values are chosen so that sufficient pressure can be transmitted onto graphene while no gas molecules penetrate the graphene sheets.

The gas pressure can be controlled by the number of gas molecules N_g and the temperature T according to Eq. (5.2). When the pressure is relatively low, the ideal gas law offers a good approximation. However, to simulate graphene nanobubbles, high pressure is often required. Moreover, since the gas volume V_g changes as the graphene sheet deforms, the pressure cannot be directly computed by Eq. (5.2). Instead, we compute the pressure from the interaction forces between gas molecules and carbon atoms, namely

$$p = \frac{1}{A} \left\langle \sum_{i=1}^{N_g} \sum_{j=1}^{N_c} F_{ij} \right\rangle \qquad (5.3)$$

where

$$F_{ij} = -\frac{\partial U_{g-c}(\mathbf{r}_{ij})}{\partial \mathbf{r}_{ij}} \cdot \mathbf{e}_z$$

is the force component in the lateral direction between gas molecule i and carbon atom j, $\mathbf{e}_z$ is the unit vector in the lateral direction, N_C is the number of carbon atoms in one of the graphene sheets, and A is the area of the graphene sheet. In the equilibrium state, the pressure is uniform in the gas phase and can be evaluated by Eq. (5.3) using either the upper or lower graphene sheet. For the upper graphene sheet, the projected area in the $x_1 - x_2$ plane is used in accordance with the force component in the z-direction, which is independent of the bubble deformation. In the present study, we use $N_c = 23,200$ and $N_g = 225,000$ to simulate graphene nanobubbles with $a = 10$ nm, while varying the temperature ($T = 10$–300 K) to achieve different pressure levels. It is assumed that the mechanical properties of graphene are insensitive to the temperature within this range [34]. Both graphene sheets are relaxed at the ground state ($T = 0$ K) before each simulation. Thermal fluctuation at a finite temperature results in a tensile residual stress (~ 0.08 N/m at 300 K). The effect of this residual stress is negligible for the present study.

Figure 1 shows an example of the MD simulation. The pressures on the upper and lower graphene sheets are calculated every 10^3 time steps by Eq. (5.3). As shown in Fig. 2(a), the two
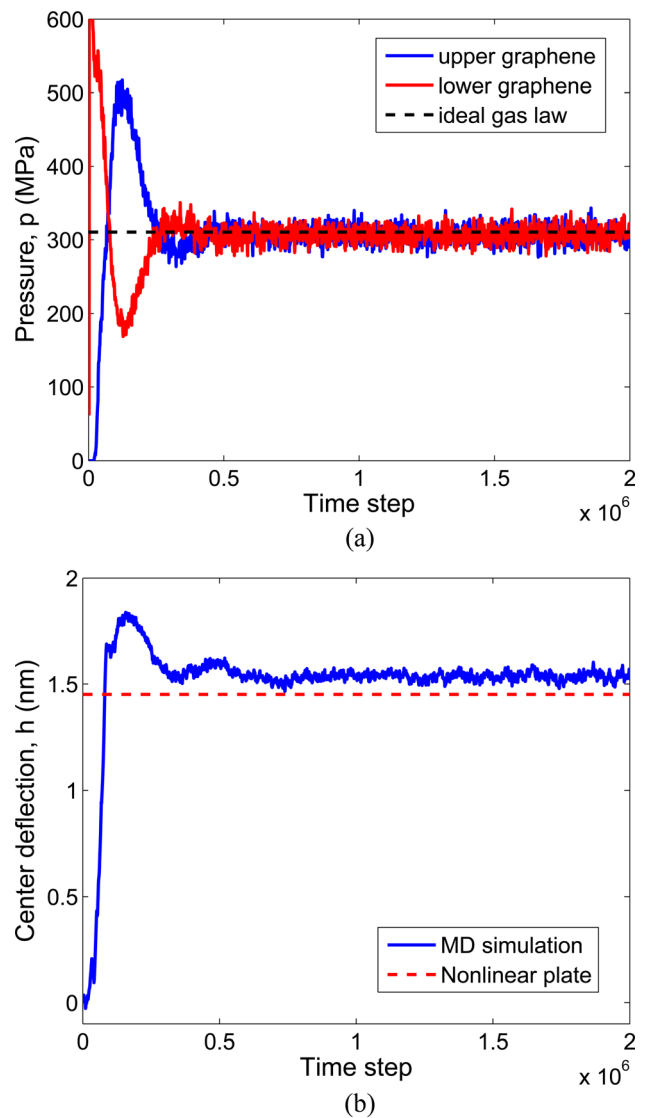

Fig. 2 (*a*) Calculated pressure in the MD simulation of a graphene bubble ($a = 10$ nm and $T = 300$ K); the dashed line is the pressure estimated by the ideal gas law. (*b*) Center deflection of the graphene bubble; the dashed line is the deflection calculated from the nonlinear plate theory using $p = 307.4$ MPa.

pressures converge after initial oscillations, indicating the thermodynamic equilibrium state of the system. The equilibrium pressure is calculated by time averaging over the last 10^6 time steps, which is slightly lower than the pressure estimated by the ideal gas law in this case. The difference is largely attributed to the increase of the gas volume under the graphene bubble, whereas the contribution of the potential energy in Eq. (5.2) is relatively small. Figure 2(*b*) shows the center deflection of the graphene bubble, which also reaches a thermodynamic equilibrium level after about 10^6 time steps. The equilibrium deflection is calculated by time averaging over the last 10^6 time steps.

6 Results and Discussions

6.1 Comparison With Analytical Solutions. Using the numerical method in Sec. 4, we calculated the deflection profiles, $w(r)$, for graphene bubbles of various radii. Figure 3 shows the normalized deflection for a graphene bubble of radius $a = 10$ nm subject to increasing pressure (without van der Waals interaction). The deflection is normalized by the center deflection, $h = w_0$. In comparison, the analytical deflection profiles in Eqs. (3.2)
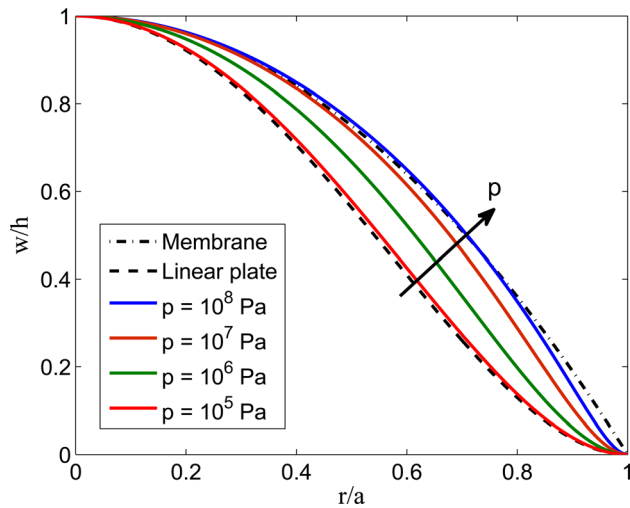
Fig. 3 Normalized deflection profiles of a graphene bubble ($a = 10$ nm) subject to increasing pressure, comparing the numerical results to the analytical solutions in Eqs. (3.2) and (3.4), from the linear plate solution and the approximate membrane analysis, respectively

and (3.4) from the linear plate solution and the approximate membrane analysis are both independent of the pressure after the normalization. The numerical result agrees well with the linear plate solution at low pressures ($<10^5$ Pa). As the pressure increases, the deflection profile approaches the membrane solution. Apparently, Eq. (3.4) is a reasonably good approximation for the deflection profile at high pressures ($>10^8$ Pa). A more accurate membrane analysis [9] would yield a better approximation but also require a numerical method. Therefore, the analytical solutions in Eqs. (3.2) and (3.4) may be considered as the lower and upper bounds for the deflection profiles.

The center deflection of a graphene bubble is a function of the pressure and the bubble radius. The linear plate solution (Sec. 3.1) predicts that the center deflection increases linearly with pressure ($h \propto p$). On the other hand, from the membrane analysis (Sec. 3.2), the cube of the center deflection increases linearly with pressure ($h^3 \propto p$). The numerical results for three different bubble radii are shown in Fig. 4(a), where the center deflection is normalized by the radius and the pressure is normalized as pa/E_{2D}. For $a = 10$ nm, the numerical results show a transition from the linear plate solution to the nonlinear membrane solution as the pressure increases. For the large bubble (e.g., $a = 1000$ nm), the numerical results are in close agreement with the membrane solution, even at very low pressures ($p \sim 0.1$ Pa). Alternatively, we plot the center deflection versus a dimensionless group, $pa^4/(E_{2D}h^3)$, as shown in Fig. 4(b). In such a plot, the numerical results for different bubble radii collapse onto one master curve. When $h > 1$ nm, the numerical results agree closely with Hencky's membrane solution, while the simple membrane analysis in Sec. 3.2 underestimates the normalized pressure. It is found that the numerical results can be fitted by a single function that is a simple sum of the linear plate solution and the membrane solution,

$$\frac{pa^4}{E_{2D}h^3} = A(\nu) + B(\nu)\left(\frac{h_e}{h}\right)^2 \qquad (6.1)$$

where A and B are two dimensionless functions of Poisson's ratio. From the membrane solution in Sec. 3.2, $A(\nu) = 1/\phi(\nu)$, which equals 2.825 for $\nu = 0.16$. On the other hand, Hencky's solution yields $A(\nu) = 3.09$ for $\nu = 0.16$. From the linear plate solution in Sec. 3.1, $B(\nu) = 16/3(1-\nu^2)$. The effective thickness, $h_e = \sqrt{12(1-\nu^2)D/E_{2D}}$, defines a length scale for the monolayer graphene. Therefore, the transition from the linear plate
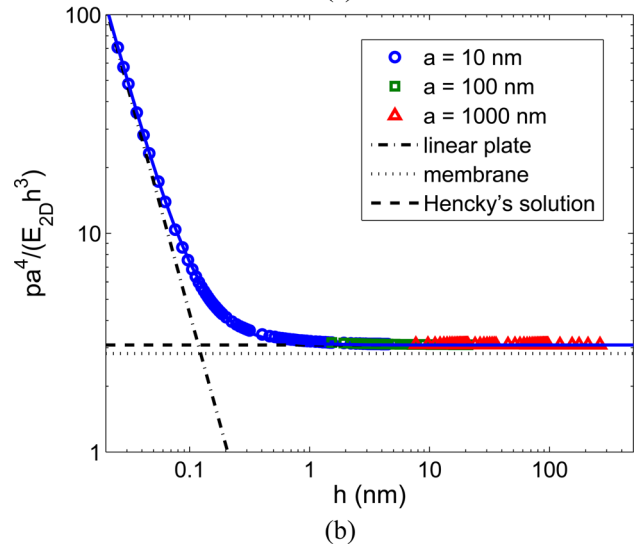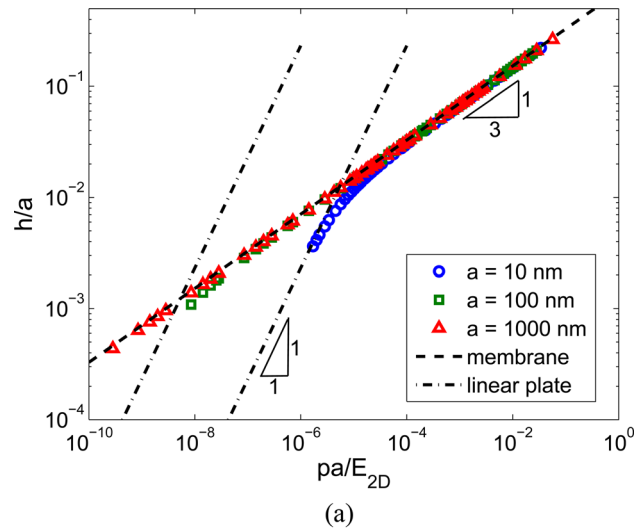

(a)

(b)

Fig. 4 (a) Normalized center deflection versus pressure for graphene bubbles; (b) normalized pressure as a function of the center deflection. The numerical results are plotted as symbols, and the analytical solutions as lines. The solid line is the fitting by Eq. (6.1) with $A = 3.09$ and $B = 5.47$.

solution to the membrane solution depends on the ratio h/h_e. For relatively large bubbles (e.g., $a > 100$ nm), since the center deflection is typically much greater than h_e, the second term on the right-hand side of Eq. (6.1) is negligible and Hencky's membrane solution is sufficient. On the other hand, for graphene nanobubbles with $h < 1$ nm such as those observed by Levy et al. [3] and Lu et al. [4], the nonlinear plate theory should be used with more accuracy.

The strain distribution is important for strain engineering as a potential approach to manipulating the electronic properties of graphene [3,4]. Figure 5 shows the strain distribution in graphene bubbles. By the symmetry and the boundary conditions, the strain is equibiaxial at the center ($r = 0$) and uniaxial at the edge ($r = a$). However, the strain distribution in between is very different from the prediction by the simple membrane analysis in Sec. 3.2. By inserting Eqs. (3.4) and (3.5) into Eqs. (2.11) and (2.12), the circumferential strain ε_θ would decrease linearly from the center to the edge, while the radial strain ε_r first decreases and then increases [8]. Moreover, the analytical membrane solution predicts that the normalized strain distribution should be independent of the pressure or the bubble radius. However, the numerical results clearly demonstrate that the strain distribution (after normalization) depends on both the pressure and the bubble radius.
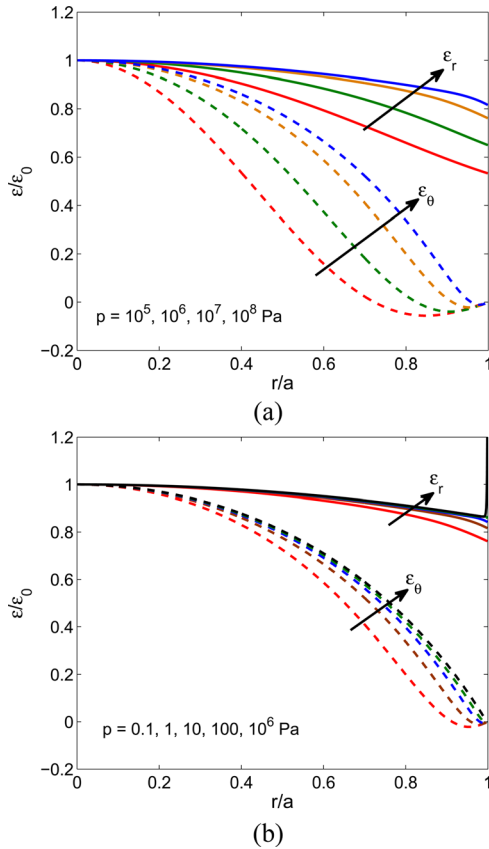
Fig. 5 Strain distributions in graphene bubbles subject to increasing pressure (*a*) *a* = 10 nm and (*b*) *a* = 1000 nm

Fig. 6 (*a*) Center strain as a function of the normalized pressure; (*b*) center strain versus *h/a*

The difference in the strain distribution between the numerical and the analytical solutions can be traced back to the difference in the deflection profiles as shown in Fig. 3. Furthermore, the in-plane radial displacement obtained by the numerical method differs from the analytical assumption in Eq. (3.5). Notably, the radial displacement becomes negative near the edge, resulting in compressive circumferential strain ($\varepsilon_\theta < 0$). Such strain distributions suggest that strain engineering with graphene bubbles is likely to be complicated.

The equibiaxial strain at the center ($\varepsilon_r = \varepsilon_\theta = \varepsilon_0$) is plotted in Fig. 6(*a*) as a function of the normalized pressure. By the membrane analysis in Sec. 3.2, we have $\varepsilon_0 = u_0/a \propto p^{2/3}$ and $\varepsilon_0 \propto (h/a)^2$. By the approximate nonlinear plate analysis in Sec. 3.3, we have $\varepsilon_0 = ac_1 \propto (h/a)^2$, and at the limit of linear plate, $\varepsilon_0 \propto p^2$. The numerical results for the graphene bubble with $a = 10$ nm shows a transition from the linear plate limit to the membrane behavior, similar to that shown in Fig. 4(*a*) for the center deflection. The numerical results for $a = 100$ and 1000 nm follow the scaling, $\varepsilon_0 \propto p^{2/3}$, but the magnitude is slightly lower than the analytical membrane solution. Noting that the center strain $\varepsilon_0 \propto (h/a)^2$ in both analytical solutions, we plot the numerical results as a function of h/a in Fig. 6(*b*). Indeed the numerical results for different bubble radii collapse onto one line with the slope 2 in the log-log plot. Therefore, the center strain may be written as

$$\varepsilon_0 = C(\nu)\left(\frac{h}{a}\right)^2 \qquad (6.2)$$

where $C(\nu)$ is a dimensionless function of Poisson's ratio. By the membrane solution in Sec. 3.2, $C(\nu) = \psi^{1/3}/\phi^{2/3}$, which equals 1.136 for $\nu = 0.16$. The numerical results can be fitted approximately by taking $C(\nu) = 0.76$. Therefore, the analytical membrane solution overestimates the center strain considerably.
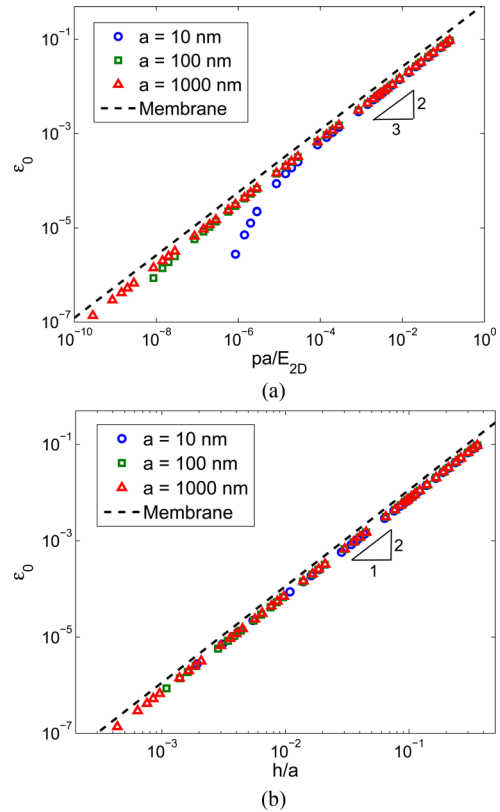
6.2 Comparison With MD Simulations. As shown in Fig. 1, a circular graphene bubble is simulated by the molecular dynamics method (Sec. 5). In the present study, only a small bubble radius ($a = 10$ nm) is considered. MD simulations of larger bubbles are computationally more demanding. By varying the temperature in the MD simulations, we calculate the deflection profiles and the corresponding pressure. Figure 7 shows the equilibrium bubble profiles, comparing the MD results with numerical solutions to the nonlinear plate equations. For this comparison, we have used $E_{2D} = 243$ N/m, $D = 1.4$ eV (or equivalently, 0.225 nN nm), and $\nu = 0.397$ in the nonlinear plate equations to match the prediction by the REBO-2 potential used in the MD simulations [10,19]. Apparently, the MD results agree closely with the nonlinear plate theory when the pressure is relatively low. At a higher pressure, the deflection from the MD simulations is higher than the prediction by the nonlinear plate theory. The center deflection as a function of the pressure is shown in Fig. 8. The discrepancy between the MD simulations and the nonlinear plate theory may be attributed to the assumption of the linear elastic properties of graphene in the continuum theory. As shown in previous studies [10–13], the elastic modulus of graphene decreases as the in-plane strain increases. As the pressure increases, the strain of graphene increases and the elastic modulus decreases in the MD simulations, resulting in larger deflections than the linear elastic model. Moreover, thermal rippling of the graphene membrane could lead to the elastic modulus at a finite temperature which is lower than the theoretical value at $T = 0$ K [35] and hence larger deflections at the higher temperatures that are used to achieve higher pressures in MD simulations. A detailed study on the effects of nonlinear elasticity and thermal rippling will be left for future work.

6.3 Effect of van der Waals Interaction. Figure 9(*a*) shows the deflection profiles of a graphene bubble ($a = 10$ nm) under the effect of vdW interaction. When the pressure is relatively low, the
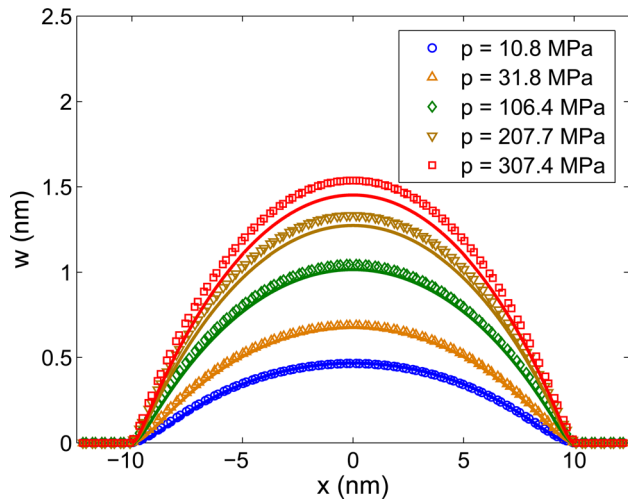
Fig. 7 Comparison of the deflection profiles for a graphene bubble ($a = 10$ nm). MD results in symbols and the numerical results from the nonlinear plate theory in solid lines.
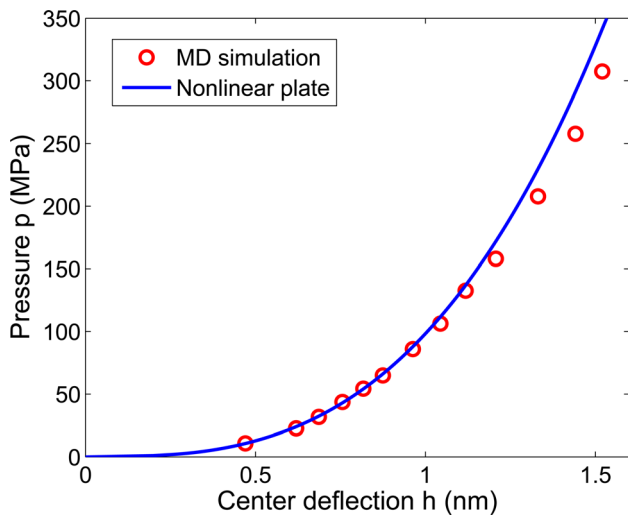

Fig. 8 Pressure versus center deflection from MD simulations of a graphene bubble ($a = 10$ nm), in comparison with the numerical solutions based on the nonlinear plate theory

(a)

(b)

Fig. 9 (a) Effect of the vdW interaction on the deflection profile of a graphene bubble ($a = 10$ nm); (b) distributions of the vdW force intensity

deflection is reduced considerably by the attractive vdW force. On the other hand, when the pressure is high, the effect of vdW force on the deflection is negligible. As shown in Fig. 9(*b*), the distribution of vdW force is nonuniform and depends on the pressure. In the spirit of nonlinear fracture mechanics [36], we may define an interaction zone where the vdW force is appreciable in comparison with the pressure, e.g., $\sigma_{vdW} > p/10$. Subject to a low pressure, the interaction zone spans the entire area underneath the bubble, indicating large-scale bridging from a fracture mechanics perspective. At a higher pressure level, the interaction zone is much smaller, where the condition of small-scale bridging prevails.

Figure 10 shows the effect of vdW interaction on the center deflection of the graphene bubble. In the presence of vdW interactions, the numerical method did not converge when the pressure is lower than a critical value (∼140 MPa). This suggests the possibility of snap-in instability, similar to snap transitions predicted for a spherical cap adhered to a rigid substrate [37]. Computationally, the Jacobian matrix in Eq. (4.5) has to be positive definite in order to converge. A more robust numerical method may be developed to further study this instability. When converged, the center deflection at a given pressure level is lower
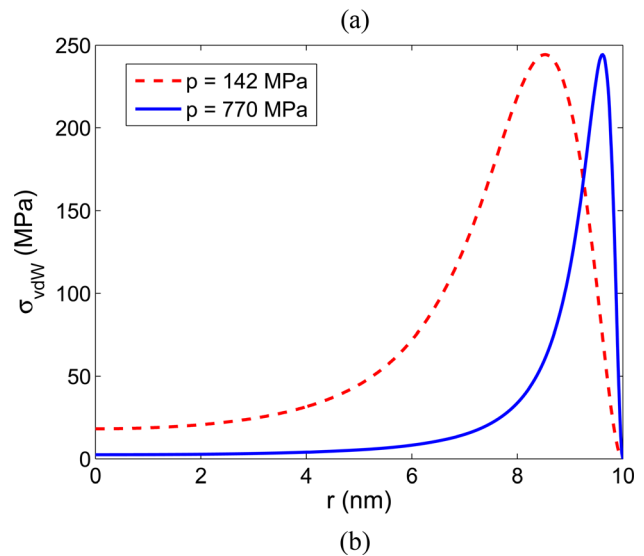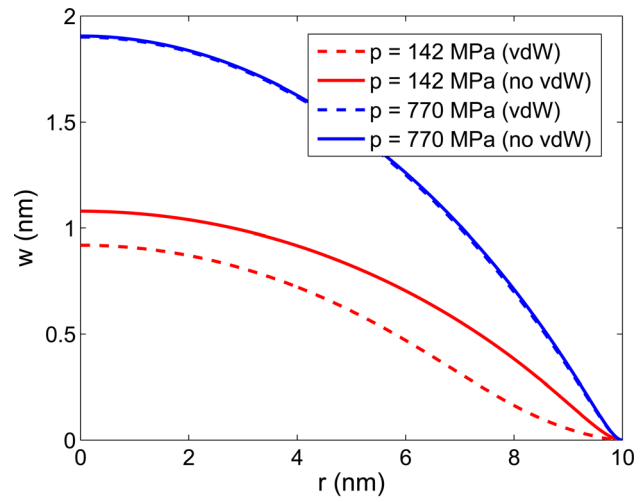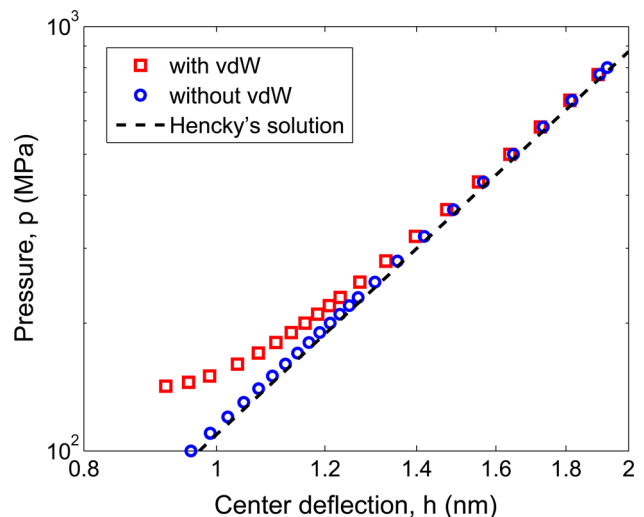

Fig. 10 Effect of the vdW interaction on center deflection of a graphene bubble ($a = 10$ nm)

in the presence of vdW interactions. As expected, the effect of vdW interactions deceases as the pressure increases and becomes negligible when $h > 1.5$ nm.

7 Conclusions

A nonlinear plate theory is adapted to describe the deformation of a graphene monolayer subject to lateral loads. A numerical method is developed to solve the nonlinear equations for circular graphene bubbles. In comparison to approximate solutions by analytical methods, it is found that the deflection profile and the strain distribution are generally not well described by the analytical solutions. Based on the numerical results, approximate formulas for the center deflection and center strain are suggested. In comparison with molecular dynamics simulations of nanoscale graphene bubbles, it is found that the continuum plate theory is suitable only within the limit of linear elasticity. On the other hand, the effect of van der Waals interactions between graphene and its substrate is found to be significant when the center deflection is relatively small.

References

[1] Stolyarova, E., Stolyarov, D., Bolotin, K., Ryu, S., Liu, L., Rim, K. T., Klima, M., Hybertsen, M., Pogorelsky, I., Pavlishin, I., Kusche, K., Hone, J., Kim, P., Stormer, H. L., Yakimenko, V., and Flynn, G., 2009, "Observation of Graphene Bubbles and Effective Mass Transport Under Graphene Films," Nano Lett., 9, pp. 332–337.
[2] Georgiou, T., Britnell, L., Blake, P., Gorbachev, R. V., Gholinia, A., Geim, A. K., Casiraghi, C., and Novoselov, K. S., 2011, "Graphene Bubbles With Controllable Curvature," Appl. Phys. Lett., 99, p. 093103.
[3] Levy, N., Burke, S. A., Meaker, K. L., Panlasigui, M., Zettl, A., Guinea, F., Castro Neto, A. H., and Crommie, M. F., 2010, "Strain-Induced Pseudo-Magnetic Fields Greater Than 300 Tesla in Graphene Nanobubbles," Science, 329, pp. 544–547.
[4] Lu, J., Castro Neto, A. H., and Loh, K. P., 2012, "Transforming Moire Blisters Into Geometric Graphene Nano-Bubbles," Nature Communications, 3, p. 823.
[5] Zabel, J., Nair, R. R., Ott, A., Georgiou, T., Geim, A. K., Novoselov, K. S., and Casiraghi, C., 2012, "Raman Spectroscopy of Graphene and Bilayer Under Biaxial Strain: Bubbles and Balloons," Nano Lett., 12, pp. 617–621.
[6] Bunch, J. S., Verbridge, S. S., Alden, J. S., van der Zande, A. M., Parpia, J. M., Craighead, H. G., and McEuen, P. L., 2008, "Impermeable Atomic Membranes From Graphene Sheets," Nano Lett., 8, pp. 2458–2462.
[7] Koenig, S. P., Boddeti, N. G., Dunn, M. L., and Bunch, J. S., 2011, "Ultrastrong Adhesion of Graphene Membranes," Nature Nanotechnol., 6, pp. 543–546.
[8] Yue, K., Gao, W., Huang, R., and Liechti, K. M., 2012, "Analytical Methods for the Mechanics of Graphene Bubbles," J. Appl. Phys., 112, p. 083512.
[9] Hencky, H., 1915, "On the Stress State in Circular Plates With Vanishing Bending Stiffness," Z. Math. Phys., 63, pp. 311–317.
[10] Lu, Q., and Huang, R., 2009, "Nonlinear Mechanics of Single-Atomic-Layer Graphene Sheets," Int. J. Appl. Mech., 1, pp. 443–467.
[11] Lee, C., Wei, X., Kysar, J. W., and Hone, J., 2008, "Measurement of the Elastic Properties and Intrinsic Strength of Monolayer Graphene," Science, 321, pp. 385–388.
[12] Wei, X., Fragneaud, B., Marianetti, C. A., and Kysar, J. W., 2009, "Nonlinear Elastic Behavior of Graphene: Ab Initio Calculations to Continuum Description," Phys. Rev. B, 80, p. 205407.
[13] Lu, Q., Gao, W., and Huang, R., 2011, "Atomistic Simulation and Continuum Modeling of Graphene Nanoribbons Under Uniaxial Tension," Modell. Simul. Mater. Sci. Eng., 19, p. 054006.
[14] Helfrich, W., 1973, "Elastic Properties of Lipid Bilayers—Theory and Possible Experiments," Z. Naturforsch. C, 28, pp. 693–703.
[15] Timoshenko, S., 1940, Theory of Plates and Shells, McGraw-Hill, New York, pp. 333–337.
[16] Kudin, K. N., Scuseria, G. E., and Yakobson, B. I., 2001, "C_2F, BN, and C Nanoshell Elasticity From Ab Initio Computations," Phys. Rev. B, 64, p. 235406.
[17] Arroyo, M., and Belytschko, T., 2004, "Finite Crystal Elasticity of Carbon Nanotubes Based on the Exponential Cauchy-Born Rule," Phys. Rev. B, 69, p. 115415.
[18] Huang, Y., Wu, J., and Hwang, K. C., 2006, "Thickness of Graphene and Single-Wall Carbon Nanotubes," Phys. Rev. B, 74, p. 245413.
[19] Lu, Q., Arroyo, M., and Huang, R., 2009, "Elastic Bending Modulus of Monolayer Graphene," J. Phys. D: Appl. Phys., 42, p. 102002.
[20] Koskinen, P., and Kit, O. O., 2010, "Approximate Modeling of Spherical Membranes," Phys. Rev. B, 82, p. 235420.
[21] Brenner, D. W., 1990, "Empirical Potential for Hydrocarbons for Use in Simulating the Chemical Vapor Deposition of Diamond Films," Phys. Rev. B, 42, pp. 9458–9471.
[22] Brenner, D. W., Shenderova, O. A., Harrison, J. A., Stuart, S. J., Ni, B., and Sinnott, S. B., 2002, "A Second-Generation Reactive Empirical Bond Order (REBO) Potential Energy Expression for Hydrocarbon," J. Phys. Condens. Matter, 14, pp. 783–802.
[23] Stuart, S. J., Tutein, A. B., and Harrison, J. A., 2000, "A Reactive Potential for Hydrocarbons With Intermolecular Interactions," J. Chem. Phys., 112, pp. 6472–6486.
[24] Plimpton, S., 1995, "Fast Parallel Algorithms for Short-Range Molecular Dynamics," J. Comput. Phys., 117, pp. 1–19.
[25] Blakslee, O. L., Proctor, D. G., Seldin, E. J., Spence, G. B., and Weng, T., 1970, "Elastic Constants of Compression-Annealed Pyrolytic Graphite," J. Appl. Phys., 41, pp. 3373–3382.
[26] Aitken, Z. H., and Huang, R., 2010, "Effects of Mismatch Strain and Substrate Surface Corrugation on Morphology of Supported Monolayer Graphene," J. Appl. Phys., 107, p. 123531.
[27] Ishigami, M., Chen, J. H., Cullen, W. G., Fuhrer, M. S., and Williams, E. D., 2007, "Atomic Structure of Graphene on SiO_2," Nano Lett., 7, pp. 1643–1648.
[28] Gupta, A., Chen, G., Joshi, P., Tadigadapa, S., and Eklund, P. C., 2006, "Raman Scattering From High-Frequency Phonons in Supported n-Graphene Layer Films," Nano Lett., 6, pp. 2667–2673.
[29] Sonde, S., Giannazzo, F., Raineri, V., and Rimini, E., 2009, "Dielectric Thickness Dependence of Capacitive Behavior in Graphene Deposited on Silicon Dioxide," J. Vac. Sci. Technol. B, 27, pp. 868–873.
[30] Zong, Z., Chen, C.-L., Dokmeci, M. R., and Wan, K.-T., 2010, "Direct Measurement of Graphene Adhesion on Silicon Surface by Intercalation of Nanoparticles," J. Appl. Phys., 107, p. 026104.
[31] Martoňák, R., Molteni, C., and Parrinello, M., 2000, "Ab Initio Molecular Dynamics With a Classical Pressure Reservoir: Simulation of Pressure-Induced Amorphization in a $Si_{35}H_{36}$ Cluster," Phys. Rev. Lett., 84, pp. 682–685.
[32] Hoover, W. G., Ross, M., Johnson, K. W., Henderson, D., Barker, J. A., and Brown, B. C., 1970, "Soft-Sphere Equation of State," J. Chem. Phys., 52, pp. 4931–4941.
[33] Clausius, R., 1870, "On a Mechanical Theory Applicable to Heat," Philos. Mag., 40, pp. 122–127.
[34] Zhao, H., and Aluru, N. R., 2010, "Temperature and Strain-Rate Dependent Fracture Strength of Graphene," J. Appl. Phys., 108, p. 064321.
[35] Chen, S., and Chrzan, D. C., 2011, "Monte Carlo Simulation of Temperature-Dependent Elastic Properties of Graphene," Phys. Rev. B, 84, p. 195409.
[36] Hutchinson, J. W., and Evans, A. G., 2000, "Mechanics of Materials: Top-Down Approaches to Fracture," Acta Mater., 48, pp. 125–135.
[37] Springman, R. M., and Bassani, J. L., 2008, "Snap Transitions in Adhesion," J. Mech. Phys. Solids, 56, pp. 2358–2380.